

Dynamical *d*-wave condensation of exciton–polaritons in a two-dimensional square-lattice potential

Na Young Kim^{1,2*}, Kenichiro Kusudo^{3,4}, Congjun Wu⁵, Naoyuki Masumoto^{3,4}, Andreas Löffler⁶, Sven Höfling⁶, Norio Kumada⁷, Lukas Worschech⁶, Alfred Forchel⁶ and Yoshihisa Yamamoto^{1,3}

Macroscopic order appears as the collective behaviour of many interacting particles. Prime examples are superfluidity in helium¹, atomic Bose–Einstein condensation², *s*-wave³ and *d*-wave superconductivity⁴ and metal–insulator transitions⁵. Such physical properties are tightly linked to spin and charge degrees of freedom and are greatly enriched by orbital structures⁶. Moreover, high-orbital states of bosons exhibit exotic orders distinct from the orders with real-valued bosonic ground states⁷. Recently, a wide range of related phenomena have been studied using atom condensates in optical lattices^{8–10}, but the experimental observation of high-orbital orders has been limited to momentum space^{11,12}. Here we establish microcavity exciton–polariton condensates as a promising alternative for exploring high-orbital orders. We observe the formation of *d*-orbital condensates on a square lattice and characterize their coherence properties in terms of population distributions both in real and momentum space.

Exciton–polaritons emerge from the strong light–matter coupling in semiconductor quantum wells embedded in a planar microcavity structure. They behave as degenerate Bose gases in the low-density and low-temperature limit¹³. Exciton–polaritons have undergone a dynamic phase transition, in which a macroscopic number of particles are accumulated in the lowest-energy single-particle state with a long-range order^{14–17}. Owing to their very light effective mass, the phase transition temperatures of exciton–polaritons are eight to nine orders of magnitude higher than those of atomic Bose–Einstein condensates. Coherence properties of exciton–polariton condensates have been characterized by the direct optical access in spatial and momentum spaces^{14–16,18}.

Modern solid-state physics has studied quantum many-body phenomena whose properties reflect exotic orbital nature, another intrinsic degree of freedom, which interplays with charge and spin degrees of freedom. Its energy degeneracy and spatial anisotropy generate rich dynamics in weakly interacting many-body systems. For example, a key role of *d*-orbital nature has been actively investigated in salient phenomena including metal–insulator transitions⁵, colossal magnetoresistance^{6,19}, and recently discovered iron-pnictide superconductors^{20,21}. These orbital ordering phenomena originate from the strong correlation effects of electrons in the anisotropic degenerate *d*-orbitals. Theoretical modelling of such

phenomena is beyond the single orbital band picture and necessarily complicated. As high-orbital bosonic condensate states can exhibit unconventional quantum order distinct from those induced by the conventional many-body ground-state wavefunctions beyond Feynman’s no-node theorem^{7,22}, the formation of designated high-orbital condensate states would pave a way to investigate exotic quantum order. Recently, a *p*-orbital condensate using ultracold atoms in an optical lattice has been prepared²³; however, to the best of our knowledge, a *d*-orbital condensate in the atom–optical lattice system has not yet been realized because of experimental difficulties. On the other hand, high-orbital bosonic condensates in the *p*- and *d*-orbital states are readily accessible in exciton–polariton systems through the bottleneck condensation dynamics by controlling the polariton density. Anti-phased *p*-orbital condensates were first demonstrated in a one-dimensional condensate array analogous to a Josephson π -junction array¹⁸, and the condensates in excited states are created in a single trap potential naturally induced by an impurity or disorder²⁴ or in a micropillar trap potential²⁵. Here we present our first demonstration of coherent anti-phased *d*-orbital condensates formed in a two-dimensional square-lattice potential. The direct natural leakage of the photons out of the microcavity allows real-space and momentum-space spectroscopy of the *d*-orbital order.

Our two-dimensional (2D) square-lattice device is patterned by depositing a thin metal film on top of a AlGaAs/AlAs planar microcavity wafer containing 12 GaAs quantum wells at the three central antinodes. The potential depth induced by the metal film is $\sim 200 \mu\text{eV}$ near zero detuning^{18,26} (see Methods for details on the device preparation and experimental set-up). We present our experimental results with a 2D square-lattice device with $a = 4 \mu\text{m}$ near zero detuning ($\sim -0.5 \text{ meV}$). We examine the spatial and the momentum distribution of microcavity exciton–polaritons in this periodic lattice potential at liquid He temperatures ($\sim 4 \text{ K}$). We excite the system using a mode-locked Ti:sapphire laser in a pulsed scheme, resonant to the excitonic branch at an energy ($\sim 767.7 \text{ nm}$) $\sim 6 \text{ meV}$ higher than the energy of the polariton ground state with $k_{\parallel} \sim 7.39 \times 10^4 \text{ cm}^{-1} \sim 5(2\pi/a)$, ten times larger than the momentum values of the first Brillouin zone edges ($\pm\pi/a$). We collect time-averaged lower polariton emission, and the far-field spectroscopy reveals the lower polariton energy–momentum

¹Edward L. Ginzton Laboratory, Stanford University, Stanford, California 94305-4085, USA, ²Institute of Industrial Science, University of Tokyo, 4-6-1 Komaba, Meguro-ku, Tokyo 153-8505, Japan, ³National Institute of Informatics, 2-1-2 Hitotsubashi, Chiyoda-ku, Tokyo 101-8430, Japan, ⁴Graduate School of Information Science and Technology, University of Tokyo, 7-3-1 Hongo, Bunkyo-ku, Tokyo 113-0033, Japan, ⁵University of California at San Diego, San Diego, California 92093, USA, ⁶Technische Physik and Wilhelm–Conrad–Röntgen–Research Center for Complex Material Systems, Universität Würzburg, D-97074 Würzburg, Am Hubland, Germany, ⁷NTT Basic Research Laboratories, 3-1 Morinosata-Wakamiya, Atsugi 243-0198, Japan.

*e-mail: nayoung@stanford.edu.

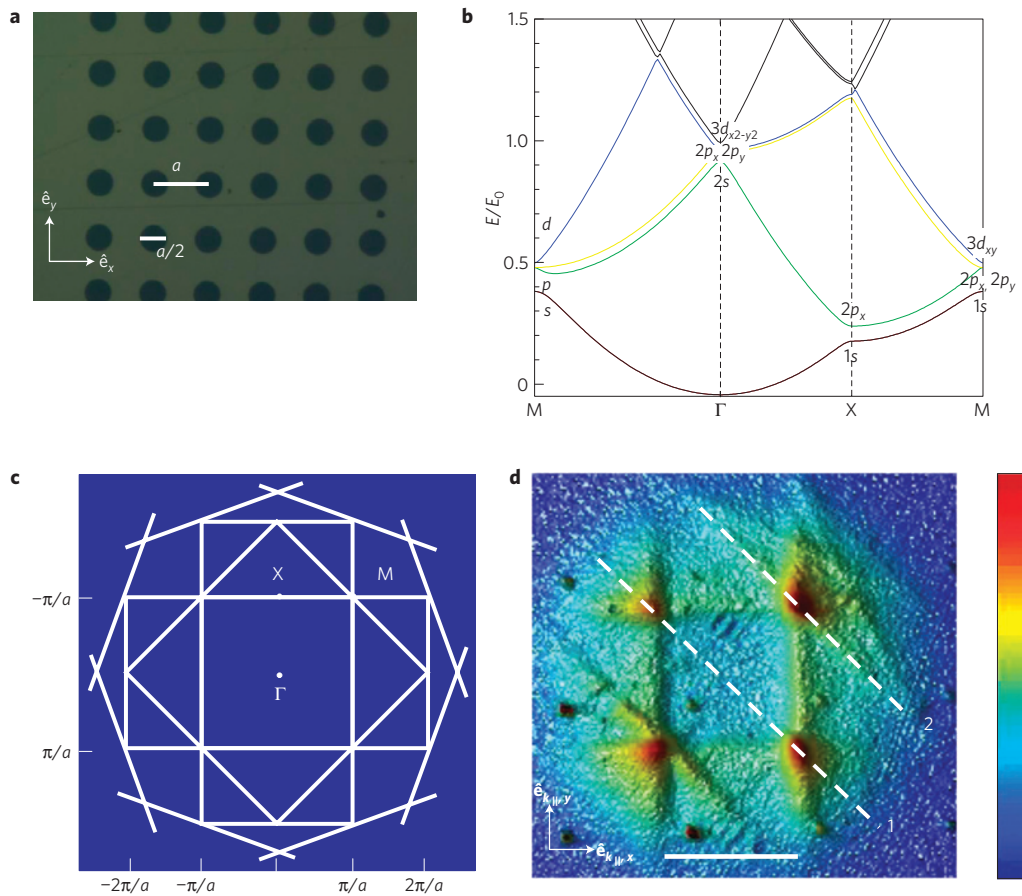


Figure 1 | Two-dimensional square-lattice device, band structure and Brillouin zones. **a**, Photograph of a 2D square-lattice structure of metal films on top of an AlGaAs/AlAs planar microcavity. A square lattice is formed by the array of circular apertures whose diameter is half the size of the lattice period a . The arrows represent the unit vectors, \hat{e}_i . **b**, The band structure of a periodic 2D square-lattice potential assuming $V_0 = 0.2E_0$, where V_0 and E_0 are the confining potential energy and the ground-state kinetic energy. **c**, Theoretical Brillouin zones of the 2D square lattice. **d**, Experimental far-field pattern corresponding to the Brillouin zones of **c**. The axis orientations of $\hat{e}_{k_{||,x}}$, $\hat{e}_{k_{||,y}}$ are given by the arrows. The dashed lines labelled 1 and 2 indicate the measurement axes for the energy–momentum dispersion (see the text). The colour scale bar shows the photoluminescence intensity strength from low (blue) to high (red) values.

dispersion curve, and the far-field imaging directly maps the Brillouin zones of the reciprocal Bravais lattices.

The estimated kinetic energies at the boundaries of the first Brillouin zone, X and M points, are $K_X(k_{||} = \pm(\pi/a)) \sim 260 \mu\text{eV}$ and $K_M(k_{||} = \pm(\sqrt{2}\pi/a)) \sim 520 \mu\text{eV}$ with an effective mass of a polariton $m^* \sim 9 \times 10^{-5} m_0$ (m_0 is the bare electron mass) and $a = 4 \mu\text{m}$. A square lattice, one of the simplest 2D lattice structures, holds translational, rotational and reflection symmetry. The reciprocal Bravais lattice is also a square pattern with a unit length $2\pi/a$. The band structures (Fig. 1b) and the 2D Brillouin zones (Fig. 1c) of a single particle with an effective mass m^* are computed with the standard plane-wave bases²⁷. Figure 1c illustrates the first four Brillouin zones, where three high-symmetry points (Γ , X, M) are specified. Experimental far-field images at a pump rate above the condensation threshold clearly identify these Brillouin zones for the $4 \mu\text{m}$ -period square lattice (Fig. 1d). Whereas both Γ and M points exhibit four-fold rotational symmetry, X points exhibit two-fold symmetry. At these high-symmetry points, the eigenstates can be classified according to their symmetry properties of the rotation group analogous to atomic orbital state denotation. At the Γ point, the lowest-energy ground state exhibits non-degenerate 1s-wave symmetry, and the next excited (quartet) states are denoted by $3d_{x^2-y^2}$, $2p_x$, $2p_y$ and $2s$ -wave symmetries in real space. It is expected that the equilibrium condensation takes place with this 1s-wave symmetry at the Γ point. Similarly, the lowest-energy (quartet) states at the M point

are split into $3d_{xy}$, $2p_x$, $2p_y$ and $1s$ —states for which the $3d_{xy}$ -wave state is only metastable, and thus it is expected that the dynamic condensation occurs with the $3d_{xy}$ -wave symmetry at the M point. Finally, the lowest-energy (doublet) states at the X point are $2p_x$ (or $2p_y$) and $1s$ states, for which the $2p_x$ (or $2p_y$) state is only metastable as a candidate for the dynamic condensation at X points.

Figure 2a shows the observed far-field images in momentum ($k_{||,x}$, $k_{||,y}$) space at various optical pump powers. These images are taken under the pump direction of $\hat{e}_{k_{||,x}} - \hat{e}_{k_{||,y}}$ ($\hat{e}_{k_{||,i}}$ are momentum space unit vectors of the configuration in Fig. 1d). This particular pump direction was chosen to access energy values of s , p and d_{xy} states individually from spectrometer measurements. Exciton–polaritons are injected at a fixed wavenumber $k_p \sim 7.39 \times 10^4 \text{ cm}^{-1}$ ($\sim 5(2\pi/a)$) even far outside the first Brillouin zone edges indicated by the red arrow in Fig. 2a. We clearly observe that different momentum distributions of exciton–polaritons emerge in a distinct order with increasing injected particle density. Below the condensation threshold pump power ($P < P_{\text{th}} \sim 7 \text{ mW}$), isotropic thermal lower polaritons leak as photons at finite $|k|$ values $\sim (2\pi/a)$ before they relax to the ground state at $(k_{||,x}, k_{||,y}) \sim 0$, giving a doughnut-shaped emission pattern (bottleneck effect). Near the condensation threshold pump power $P \sim P_{\text{th}}$, the metastable $3d_{xy}$ state at M points, $(k_{||,x}, k_{||,y}) = (\pm\sqrt{2}\pi/a, \pm\sqrt{2}\pi/a)$, of the first Brillouin zone is selectively occupied as expected. The injected exciton–polaritons with the initial momentum

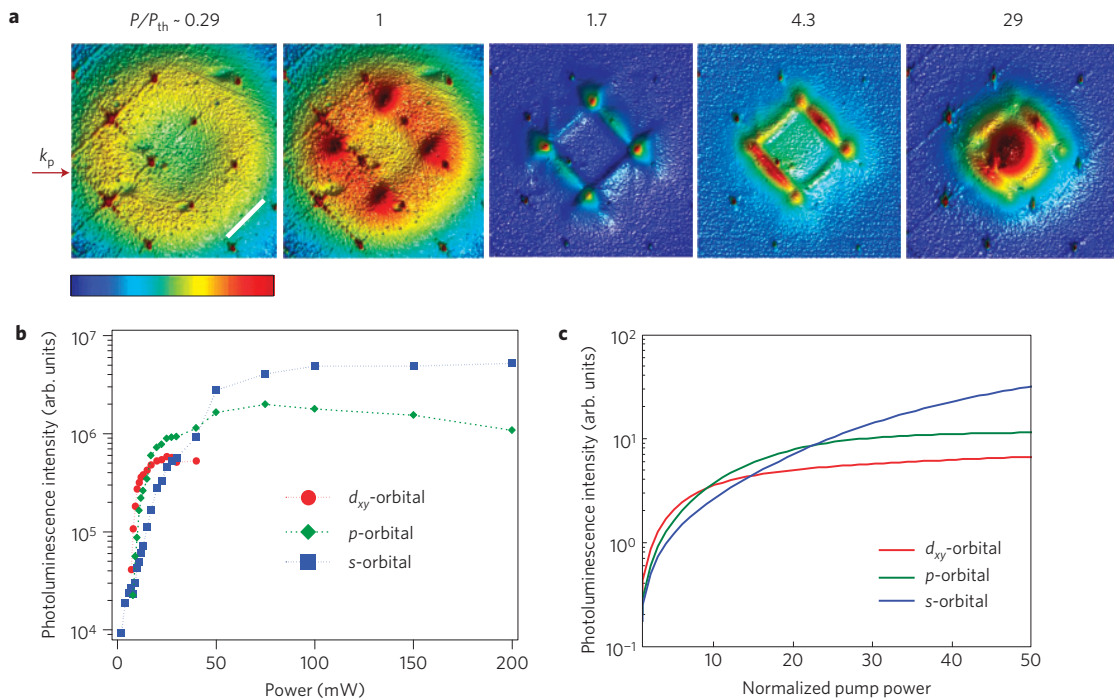


Figure 2 | Lower polariton distribution in reciprocal lattice space. **a**, Pump-power-dependent far-field images for the pumping direction along $\hat{e}_{k_{\parallel,x}} - \hat{e}_{k_{\parallel,y}}$. The relative pump rates (P/P_{th}) are 0.29, 1, 1.7, 4.3 and 29. The narrow peaks in the square-lattice positions originate from pump laser scatterings by the periodic circular aperture, whose distance provides the size of the first Brillouin zone, $2\pi/a$ (white bar), empirically with a 0.5% error due to the difference in the laser wavelength and polariton wavelength. **b**, The population of $1s, 2p_x$ and $3d_{xy}$ -orbital states plotted against the pump power. **c**, Numerical simulation results of integrated lower polariton photoluminescence intensity of the $1s, 2p_x$ and $3d_{xy}$ -orbital states against the normalized pump power.

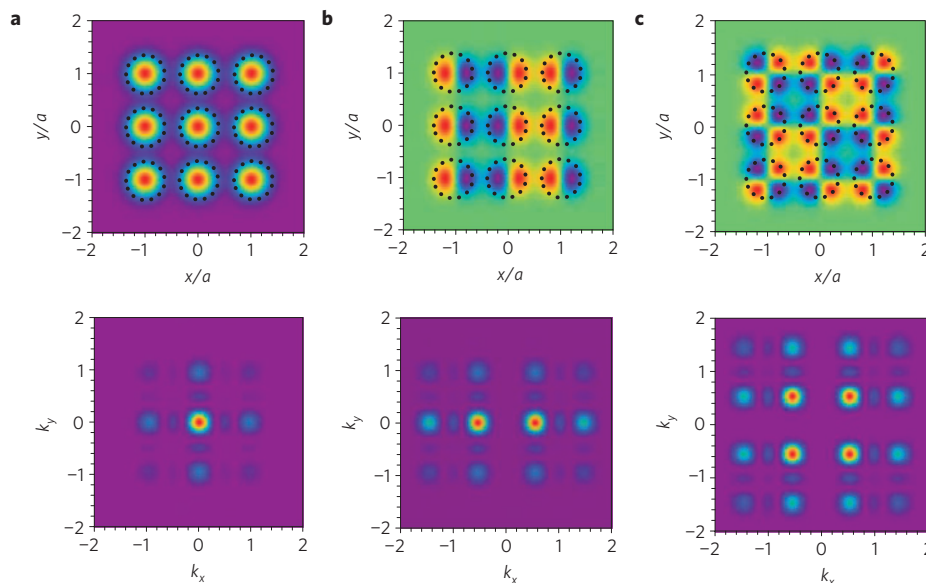


Figure 3 | Theoretical near-field and far-field patterns in a strong potential. The calculation assumed a strong harmonic potential trap, and the near-field (top) and far-field (bottom) wavefunctions for the $1s$ (**a**), $2p_x$ (**b**) and $3d_{xy}$ (**c**) orbital condensates are presented, where the red (blue) colour indicates positive (negative) amplitudes in real-space wavefunctions. The positions of circular traps (apertures) on the device surface are indicated by dotted circles. Whereas $1s$ -orbital wavefunctions are connected in-phase between lattice sites, both $2p_x$ and $3d_{xy}$ wavefunctions are connected in an anti-phased manner. The square of the far-field wavefunction or the momentum distribution of the three condensates is also shown. The anti-phased $2p_x, 3d_{xy}$ wavefunctions in real space induce interference peaks at the X and M points, respectively, in momentum space. The calculation results in the case of the weak trap potential are given in the Supplementary Information.

$k_{\parallel,x} = k_{\parallel,y} \sim 7.39/\sqrt{2} \times 10^4 \text{ cm}^{-1} \sim 4.7(\sqrt{2}\pi/a)$ relax and dynamically condense at M points. As the pump rate increases, the momentum spread Δk at M points markedly decreases, indicating that a phase order is formed over a macroscopic distance $\sim 40 \mu\text{m}$.

With a further increase of the pump rate, the condensation in the metastable $2p_x$ state at X points and finally the condensation in the $1s$ ground state at the Γ point are observed. The crossover behaviour among the $3d_{xy}, 2p_x$ and $1s$ states for varying pump rates is presented

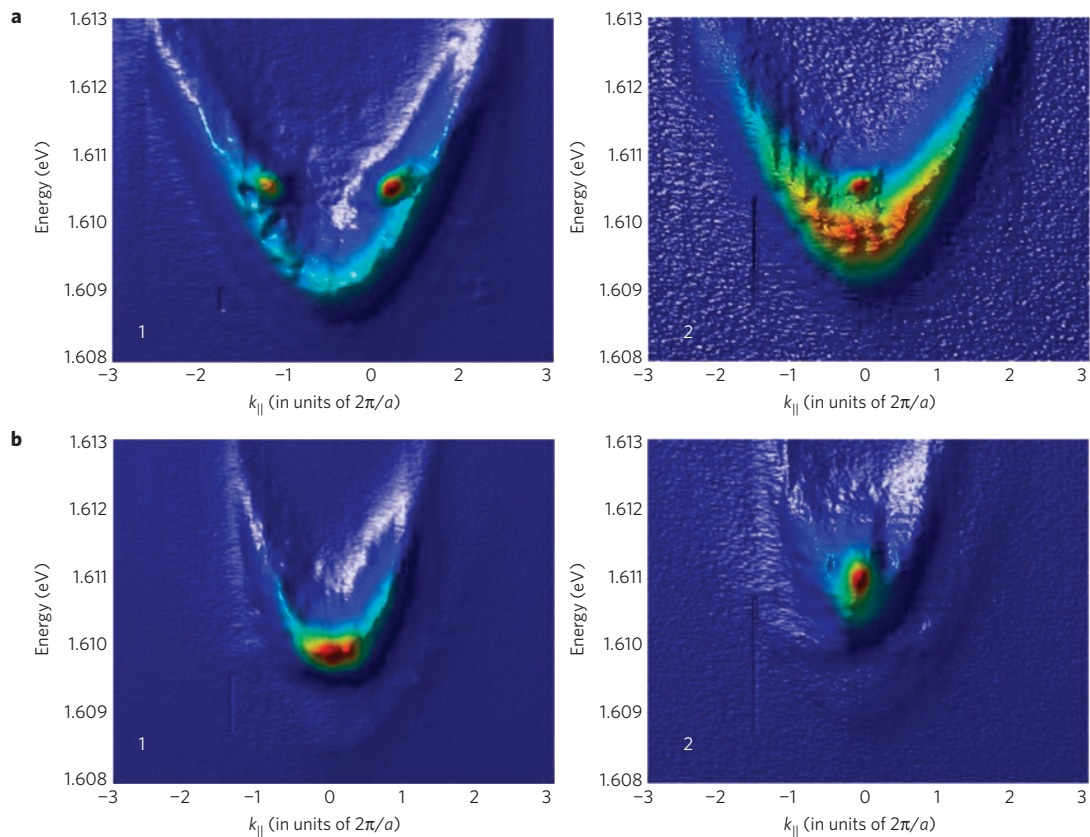


Figure 4 | Energy-momentum dispersion characteristics. The cross-sectional energy-momentum dispersion relations are measured along lines 1 and 2 in Fig. 1d. Line 1 (left column) follows the high-symmetry point Γ -M direction of the first Brillouin zone and line 2 (right column) examines the edge of the second Brillouin zone around the M point. Experimental data are taken at $P/P_{\text{th}} = 1$ ($P_{\text{th}} = 7$ mW; **a**) and $P/P_{\text{th}} \sim 7$ (**b**), presented on a linear intensity scale. Along line 1, we have extracted the energy values and the population of the $1s$ and $3d_{xy}$ condensate states in terms of the pump power. The same information for the $2p_x$ condensate states between lines 1 and 2 is presented in Supplementary Fig. S2. The nonlinear increases for $1s$, $2p_x$ and $3d_{xy}$ condensate populations are given in Fig. 2c. Distinct signals from M points along line 2 in **b** appear even at high power values, whereas the dominant $1s$ condensate signals mask the signals at M points along line 1 in **b**.

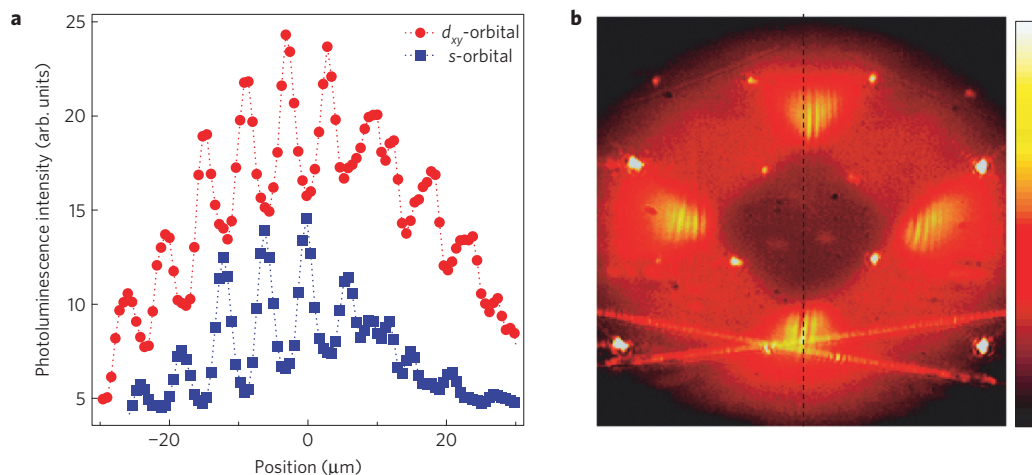


Figure 5 | Energy-resolved spatial characteristics. **a**, Cross-sectional intensity profile at two energy eigenvalues, 1,609.64 meV ($3d_{xy}$ orbital, red) and 1,608.76 meV ($1s$ orbital, blue). **b**, Interference fringe at $P/P_{\text{th}} = 1$ observed in a far-field plane from Michelson interferometry, in which one arm has a standard mirror and the other has a right-angle prism for folding an image along the centre (dashed line).

in Fig. 2b. As our initial laser momentum is ten times larger than the first Brillouin zone edge, a significant incoherent scattering process by acoustic phonons should be involved to relax into the first Brillouin zone. Consequently, the coherence of the d - and p -band is established spontaneously. Figure 2c shows that this dynamical

competition among states is well captured by a simple theoretical model using the coupled rate equations with a reasonable decay rate of an individual state.

The far-field interference patterns manifest the relative phase between the real-space Bloch wavefunctions of the orbital

symmetry. We compute the real-space wavefunction configurations (near-field images) and the momentum distribution (far-field images). Figure 3 shows the strong parabolic trap potential case in a 3-by-3 lattice site, where real-space wavefunctions are tightly localized at each site, which elucidate clearly the near-field orbital symmetry (the near-field wavefunctions and the far-field distribution in a weak trap potential case, which are more relevant to our experimental condition, are presented in the Supplementary Information). The $1s$ ground state is stable at the Γ point, the metastable $2p_x$ states appear at X points and the metastable $3d_{xy}$ states appear at M points. The anti-phased $3d_{xy}$ -orbital symmetry between nearest-neighbour sites is the reason for the intensity peaks at M points in momentum space in Fig. 3c. Similarly, the anti-phased $2p_x$ states are responsible for the intensity peaks at X points in Fig. 3b. On the other hand, the conventional in-phased $1s$ -orbital condensate produces the intensity peak at the Γ point in Fig. 3a. Multiple side peaks in the far-field patterns in Fig. 3 arise from the tightly localized wavefunction per site in the strong potential case, whereas only the first-order interference peaks appear in the weak potential case (Supplementary Information). In our experimental results presented in Fig. 2a, the interference patterns created by the $1s$ and $2p_x$ orbitals are broader in momentum space compared with that created by the $3d_{xy}$ orbitals. This feature implies that the $1s$ and $2p_x$ orbitals are less coherent than the $3d_{xy}$ orbitals in real space. This is a direct consequence of the larger tunnelling coupling between sites for the $3d_{xy}$ state.

To quantify the energy eigenvalues of the three orbital states, we carry out the spectroscopic measurement of the energy–momentum dispersion relation by selecting a particular cross-section in momentum space (Fig. 4a,b). Selected cross-sections are along the lines indicated by diagonal lines with numbers 1 and 2 in Fig. 1d. The $1s$ and $3d_{xy}$ orbitals are observed in line 1, whereas only the $3d_{xy}$ orbital is observed in line 2. From the pump-power dependence of the observed energy–momentum dispersion curves, we extract two quantities: the energy eigenvalues and the 2D in-plane wavenumbers of individual orbital states. Along line 1, the distance between two prominent peaks ($3d_{xy}$ -orbital states) corresponds to the diagonal length of the first Brillouin zone ($2\pi\sqrt{2}/a$), and the energy of these states lies at $E_{3d_{xy}}(M) \sim 1,610.55$ meV near the threshold pump, $P_{th,d} = 7$ mW (Fig. 4a, left). The $1s$ ground-state energy at $(k_{||,x}, k_{||,y}) = (0, 0)$ is $E(0) \sim 1,608.93$ meV below the condensation threshold, but this s -orbital state also condenses at $E_s(0) \sim 1,609.83$ meV at the slightly higher threshold power $P_{th,s} = 10$ mW. An energy blueshift (~ 0.9 meV) is due to the repulsive polariton–polariton interactions. The $E_{3d_{xy}}(M)$ at line 2 is identical to that of the $3d_{xy}$ state along line 1 (Fig. 4a, right) as expected. Near the threshold pump power, the energy eigenvalues of the $1s$ state at the Γ point, $2p_x$ state at X points, and $3d_{xy}$ states at M points are equally spaced by 0.36 meV, which is compatible with the theoretically expected energy spacing ~ 0.26 meV within 30% error. At higher pump power, lower polaritons at high-orbital states are further relaxed into smaller $k_{||}$ -valued states, and Fig. 4b shows some representative data at $P \sim 50$ mW $\sim 7P_{th}$.

We execute spatially resolved spectroscopy and capture the near-field images, from which the $3d_{xy}$ -orbital condensation is confirmed. The cross-sectional cuts at two energy eigenvalues (s (blue) and d (red) orbitals) along the $\hat{e}_x + \hat{e}_y$ direction (\hat{e}_i are real-space unit vectors of the configuration in Fig. 1a) show the anti-correlated emission profiles in spatial coordinates for the $1s$ -orbital condensate and $3d_{xy}$ -orbital condensates (Fig. 5a). A similar result is obtained along the $\hat{e}_x - \hat{e}_y$ direction, which unambiguously confirms the $3d_{xy}$ symmetry of the real-space Bloch wave. Phase coherence of the $3d_{xy}$ -orbital condensate is further confirmed by a Michelson interferometer constructed in momentum space. We place a simple mirror and a right-angle prism at each arm of the Michelson interferometer to fold the far-field

images with respect to the centre line. Figure 5b shows that the interference fringes indeed exist only at M points near $P \sim P_{th}$. This result rules out the independent condensation at four M points (condensate fragmentation in momentum space) but supports our previous discussion that the dynamic condensation takes place with the anti-phased $3d_{xy}$ -wave symmetry over many sites.

Methods

Sample preparation. Our wafer is grown by molecular beam epitaxy on a (100)-oriented GaAs substrate. We have placed three four-fold stacks of 7-nm-thick quantum wells separated by 3-nm-thick AlAs barriers at the three central antinodes of the microcavity. The wafer displays an exciton–polariton splitting of ~ 13.6 meV at zero detuning, and the cavity resonance energy is tapered for the detuning parameter adjustment. An electrostatic in-plane trap potential in a 2D square-lattice geometry is produced by depositing a thin Au/Ti (25/3 nm) film on a lithographic pattern (Fig. 1a). The pattern arranges circular apertures with a period of a , where $a/2$ is the diameter of the aperture.

Experimental set-up. The sample was optically pumped by a mode-locked Ti:sapphire laser, focused to a 60-by-120 μm^2 spot. A circularly polarized 3 ps pulse is injected at an incident angle of 60° (corresponding to the in-plane wavenumber, $k_{||} \sim 7.39 \times 10^4 \text{ cm}^{-1} \sim 5(2\pi/a)$) with a 76 MHz repetition rate. We collect time-averaged lower polariton emission through a 0.55 NA microscope objective lens, fed into either a 750 mm grating spectrometer with a nitrogen-cooled CCD (charge-coupled device) for spectroscopy or a CCD camera for imaging.

Received 22 December 2010; accepted 5 May 2011;
published online 19 June 2011

References

- Leggett, A. J. *Quantum Liquids: Bose Condensation and Cooper Pairing in Condensed-Matter Systems* (Oxford Univ. Press, 2006).
- Pitaevskii, L. P. & Stringari, S. *Bose–Einstein Condensation* (Clarendon, 2003).
- Tinkham, M. *Introduction to Superconductivity* (McGraw-Hill, 1996).
- Van Harlingen, D. J. Phase-sensitive tests of the symmetry of the pairing state in the high-temperature superconductors—evidence for $d_{x^2-y^2}$ symmetry. *Rev. Mod. Phys.* **67**, 515–535 (1995).
- Imada, M., Fujimori, A. & Tokura, Y. Metal–insulator transitions. *Rev. Mod. Phys.* **70**, 1039–1263 (1998).
- Tokura, Y. & Nagaosa, N. Orbital physics in transition-metal oxides. *Science* **288**, 462–468 (2000).
- Wu, C. Unconventional Bose–Einstein condensations beyond the ‘no-node’ theorem. *Mod. Phys. Lett. B* **23**, 1–24 (2009).
- Greiner, M. *et al.* Quantum phase transition from a superfluid to a Mott insulator in a gas of ultracold atoms. *Nature* **415**, 39–44 (2002).
- Paredes, B. *et al.* Tonks–Girardeau gas of ultracold atoms in an optical lattice. *Nature* **429**, 277–281 (2004).
- Chin, J. K. *et al.* Evidence for superfluidity of ultracold fermions in an optical lattice. *Nature* **443**, 961–964 (2006).
- Müller, T., Fölling, S., Widera, A. & Bloch, I. State preparation and dynamics of ultracold atoms in higher lattice orbitals. *Phys. Rev. Lett.* **99**, 200405 (2007).
- Köhl, M., Moritz, H., Stöferle, T., Günter, K. & Esslinger, T. Fermionic atoms in a three dimensional optical lattice: Observing Fermi surfaces, dynamics, and interactions. *Phys. Rev. Lett.* **94**, 080403 (2005).
- Kavokin, A. & Malpuech, G. *Cavity Polaritons* (Academic, 2003).
- Deng, H. *et al.* Condensation of semiconductor microcavity exciton polaritons. *Science* **298**, 199–202 (2002).
- Kasprzak, J. *et al.* Bose–Einstein condensation of exciton polaritons. *Nature* **443**, 409–414 (2006).
- Balili, R. *et al.* Bose–Einstein condensation of microcavity polaritons in a trap. *Science* **316**, 1007–1010 (2007).
- Bajoni, D. *et al.* Polariton laser using single micropillar GaAs–GaAlAs semiconductor cavities. *Phys. Rev. Lett.* **100**, 047401 (2008).
- Lai, C. W. *et al.* Coherent zero-state and π -state in an exciton–polariton condensate array. *Nature* **450**, 529–533 (2007).
- Salamon, M. B. & Jaime, M. The physics of manganites: Structure and transport. *Rev. Mod. Phys.* **73**, 583–628 (2001).
- Ishida, K., Nakai, Y. & Hosono, H. To what extent iron-pnictide new superconductors have been clarified: A progress report. *J. Phys. Soc. Jpn* **78**, 062001 (2009).
- Mazin, I. I. & Schmalian, J. Pairing symmetry and pairing state in ferropnictides: Theoretical overview. *Physica C* **469**, 614–627 (2009).
- Feynman, R. P. *Statistical Mechanics: A Set of Lectures* (Addison-Wesley, 1972).
- Wirth, G., Ölschläger, M. & Hemmerich, A. Evidence for orbital superfluidity in the P -band of a bipartite optical square lattice. *Nature Phys.* **7**, 147–153 (2010).
- Sanvitto, D. *et al.* Exciton–polariton condensation in a natural two-dimensional trap. *Phys. Rev. B* **80**, 045301 (2009).

25. Maragkou, M. *et al.* Spontaneous nonground state polariton condensation in pillar microcavities. *Phys. Rev. B* **81**, 081307 (2010).
26. Kim, N. Y. *et al.* GaAs microcavity exciton–polaritons in a trap. *Phys. Status. Solidi B* **245**, 1076–1079 (2008).
27. Ashcroft, N. W. & Mermin, N. D. *Solid State Physics* (Brooks Cole, 1989).

Acknowledgements

We acknowledge Special Coordination Funds for Promoting Science and Technology in Japan, Navy/SPAWAR Grant N66001-09-1-2024, MEXT, the Japan Society for the Promotion of Science (JSPS) through its Funding Program for World-Leading Innovative R&D on Science and Technology (FIRST Program), and State of Bavaria. C.W. is supported by the NSF under grant no. DMR-0804775.

Author contributions

Y.Y. and N.Y.K. conceived this study. A.L. and S.H. grew the wafer. K.K. processed the device. N.Y.K. built an optical set-up, and N.Y.K., K.K. and N.M. carried out experiments. N.Y.K. and Y.Y. analysed experimental data and C.W. carried out band-structure calculations. N.Y.K. and Y.Y. wrote the manuscript. All authors discussed the results and commented on the manuscript.

Additional information

The authors declare no competing financial interests. Supplementary information accompanies this paper on www.nature.com/naturephysics. Reprints and permissions information is available online at <http://www.nature.com/reprints>. Correspondence and requests for materials should be addressed to N.Y.K.